Cellulose nanofiber nanocomposites with aligned silver nanoparticles

Ito, Hiroaki

Sakata, Mibuki

Hongo, Chizuru

Matsumoto, Takuya

Nishino, Takashi

Cellulose nanofiber nanocomposites with aligned silver nanoparticles
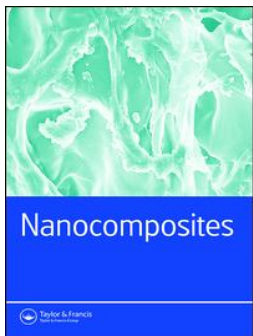
Hiroaki Ito, Mibuki Sakata, Chizuru Hongo, Takuya Matsumoto & Takashi Nishino

View supplementary material

Published online: 02 Jan 2019.

Submit your article to this journal

Article views: 398

View Crossmark data

Cellulose nanofiber nanocomposites with aligned silver nanoparticles

Hiroaki Ito, Mibuki Sakata, Chizuru Hongo, Takuya Matsumoto and Takashi Nishino

Department of Chemical Science and Engineering Graduate School of Engineering, Kobe University, Rokko, Nada, Kobe, Japan

ABSTRACT

Celluloses have attracted much attention as sustainable and abundant materials. Herein, we focus on nanocomposites based on the oxidation-treated nano-sized fibrillated celluloses, namely TOCNs. The silver nanoparticles (AgNPs) were prepared in TOCN aqueous dispersion. Generally, the AgNPs are quickly agglomerated after preparation. For the inhibition of the agglomeration of AgNPs, it is required that AgNPs were prepared under the chelation of TOCN, followed by reduction therein. Therefore, AgNPs possessed the nano-scaled radii and aligned along the TOCN from the atomic force microscopic measurements. The thermal stabilities and mechanical properties were increased. The anisotropic thermal conductivities originated from the orientation of TOCN in nanocomposites were observed. The loading of the large amounts of AgNP fillers led to the drastic increase of the thermal and electrical conductivities. The conductive paths of heat and electron were formed by the contact of AgNP with each other. We functionalized the TOCN papers through the loading of AgNPs and the obtained nanocomposites sheets served as conductors.
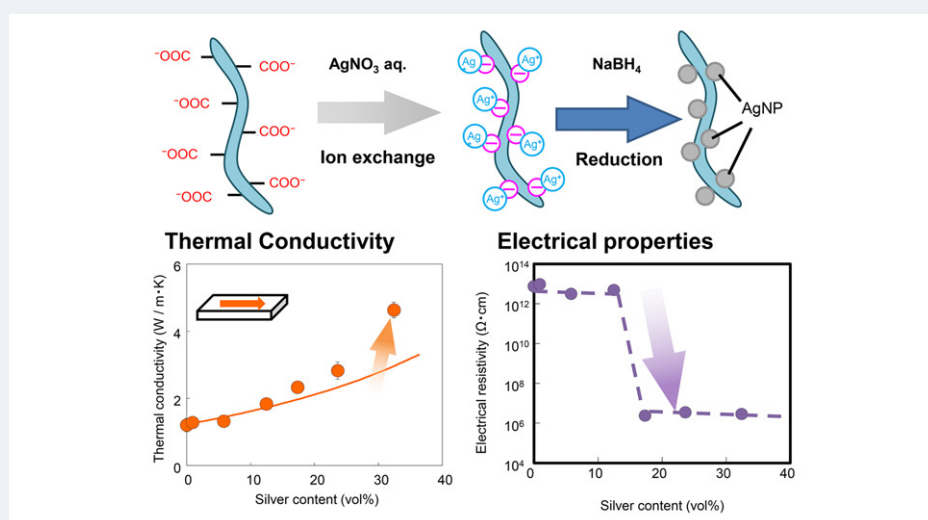
Introduction

In our daily life, petroleum-resource-based synthetic polymers, such as polyolefins, polystyrene and poly-vinylchloride have widely spread. However, for these decades, the environmental problems such as global warming and exhaustible resources have been arisen. Cellulose is the most abundant, sustainable and environmental-friendly natural product in the world and attracts much attentions as an alternative material to synthetic polymers in the field of not only agriculture but also polymer science [1]. In addition, it has been reported that isotropic sheet composed of cellulose nanofibers (CNFs) possesses much higher elastic modulus than 10 GPa [2–5]. Therefore, CNFs are well known as remarkable materials with high mechanical properties, light weight, low linear thermal expansion coefficient, biocompatibility and high specific surface [6–11]. CNFs are accepted as fillers in nanocomposites [12, 13], substrates of electrical devices [14–18],

CONTACT Takashi Nishino tnishino@kobe-u.ac.jp Department of Chemical Science and Engineering Graduate School of Engineering, Kobe University, Rokko, Nada, Kobe, Japan

wrapping papers with high performance [19, 20] and scaffolds for tissue engineering [21, 22]. CNFs are prepared in the two different typical methods; one is the mechanical method such as grinding processes [23, 24] and the other is the chemical method such as 2,2,6,6-tetramethylpiperidine-1-oxyl (TEMPO)-mediated oxidation [25–27]. In particular, the TEMPO treatment selectively and densely introduces carboxyl groups to the 6-positions of a half of glucopyranose rings at the surface of cellulose nanofibers. The nanofibers of TEMPO-oxidized CNFs (TOCNs) show high aspect ratios with radii of about 3–5 nm and lengths of several micro meters. These low radius and high aspect ratio lead to the increasing of entanglements and the decreasing defects of CNFs. Therefore, they improve mechanical properties relative to micro-fibrillated CNF.

In organic–inorganic nanocomposites, where organic matrices are reinforced and functionalized by the nanosized inorganic fillers, the higher performance and functionality have been achieved; for example, mechanical properties [28–30], gas permeabilities [31, 32], higher thermal and electrical conductivities [33–36] and the control of refractive indexes [37–40]. Various inorganic nanofillers for the nanocomposites have been reported. Silver nanoparticles (AgNPs) exhibit catalytic activities [41–43], surface-enhanced Raman scattering activities [44–46], high electrical and thermal conductivities [47, 48] and antimicrobial activities [49, 50]. In the case of nanocomposites, the dispersibility of nanofillers in polymer matrix is a key factor for the achievements of their high performance because of rapid and easy agglomeration of nanofillers in dispersion. For the well-dispersion of AgNPs, it has been reported on the usage of surfactant and *in situ* preparation methods. Among them, the well-dispersed AgNPs are often prepared in the *in situ* synthesis through the reductive reaction of metal ions. Moreover, the *in situ* synthesis by chelation to metal ions leads to the inhibition from random agglomeration as well as the 1D and 2D arrangements of AgNPs along polymer chains and sheets [51–53]. These arrangements induce the percolation of the contacts of nanofillers, the anisotropy of the functional properties and the drastic increase of electrical conductivity with the low loading of nanofillers.

Herein, we focused on TOCN/AgNP nanocomposites and investigated their mechanical and functional properties. The AgNPs were prepared from Ag cation in TOCN aqueous dispersion. In the TOCN dispersion, the Ag ions were chelated with the carboxylate groups at the 6-position of cellulose, and then they are reduced to AgNPs on the TOCN [54, 55]. AgNPs are agglomerated rapidly without

any dispersion stabilizers, whereas the chelation effects of TOCN made the high dispersity of AgNPs possible. We observed well-dispersed and aligned AgNPs with atomic force microscope (AFM). In addition, we evaluated the reinforcement effects of AgNP fillers and anisotropic functional properties through investigation on their mechanical properties as well as functional properties such as Young's modulus, thermal conductivities and electrical conductivities.

Experimental

Materials

Kenaf bast fibers (*Hibiscus cannabinus*, Indonesia, 2011) with 2 mm of the average length were provided from Toyota Boshoku co. (Aichi, Japan). All the chemical reagents were purchased with chemical company.

Purification of kenaf bast fibers

Kenaf bast fibers, 20 g, were degreased via Soxhlet extraction using a 1:2 (v/v) mixture of ethanol/toluene for 20 h at 130 °C. Kenaf bast fibers then were dried for 2 days under ambient atmosphere before a half of the degreased biomass was suspended into 1 L of distilled water. For removing the lignin of the sample with Wise method, sodium chlorite, 6.7 g and acetic acid 1.2 mL were directly added to the biomass suspension. The biomass suspension mixture was heated at 80 °C for 1 h. The addition of sodium chlorite, 6.7 g, and acetic acid, 1.2 mL, was repeated four times in 1 h intervals. The mixture was filtered and suspended into distilled water five times. In order to remove the hemicellulose, the biomass samples were suspended in 0.5 L of 4 wt% KOH aq. and stirred for 2 h at 80 °C. Following that, the refined biomass was washed through 5 times filtration and resuspension. Three times of these alkali treatments provided the refined pulp.

TEMPO oxidation treatment

The above refined pulp 10 g, TEMPO 156 mg and NaBr 1.0 g were added into 1 L distilled water. 25 mL sodium hypochlorite solution was added slowly keeping below pH 10 by the automatic titrator. When the constant increase of pH of the solution with addition of 0.5 M NaOH aqueous solution was achieved, the oxidation was stopped. Following that, the oxidized biomass were washed through the five times filtration and redispersion.

The semi-wetted biomass samples were suspended in 1 L acetate buffer solution with pH 4.8. The sodium chlorite was added with the ratio of
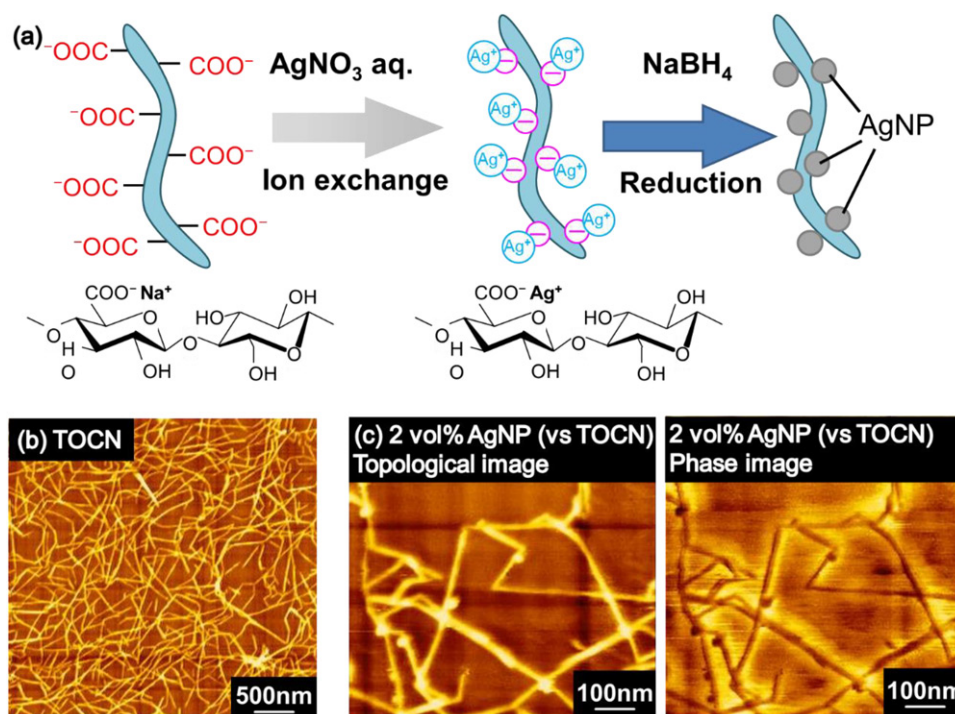
Figure 1. (a) Preparation scheme of AgNPs along the TOCN and the AFM topological (left) and phase (right) images of (b) TOCN and (c) TOCN/AgNPs nanocomposites.

1.14 g for 1 g biomass and stirred for 48 h. Following that, the oxidized biomass were washed through the five times filtration and redispersion. These two reactions led to the oxidation of cellulose.

The oxidized biomass pulps dispersed into 700 mL water were fibrillated by the blending mixer with 24,000 rpm for 10 min. The TOCNs were obtained.

Preparation of silver nanoparticles in TOCN suspension

For 215 g of the 0.25 wt% TOCN aqueous dispersion, the silver nitrate aqueous solution was added, which amounts were equal to the 0.3–30 vol% silver against TOCN after reduction. The suspensions were stirred for 1 day under darkness and the ion exchanges were proceeded. 3.2 wt% sodium borohydride aqueous solution with the equivalent to the silver nitrate was added and stirred for 1 day. The reduction of silver ions led to the formation of AgNPs in the TOCN dispersion.

Preparation of TOCN and TOCN/AgNP nanocomposite sheets

After defoaming of TOCN or TOCN/AgNP suspension, the suspensions containing 0.65 g of TOCN were filtered and the sheets were obtained. The sheets were dried under vacuum at 40 °C. All the procedures were shown in Figure S1 in the Supporting Information.

Characterization

Infrared absorption (FT-IR) spectroscopy was carried out on Spectrum GX FT-IR System I-KS (Perkin Elmer co. ltd.). The samples were dispersed into KBr and were dried for 24 h at 40 °C.

In order to estimate the amount of carboxyl groups in TOCN, the electrical conductivity and pH curves were measured by acid–base titration with an automatic titrator (AUT-501, TOA-DKK Co. Ltd.) and an electrical conductometer (CM-60V, TOA-DKK Co. Ltd.).

The radii of TOCN and AgNPs were measured by atomic force microscopy Nano Navi II E-sweep (SII nanotechnology Co. Ltd.) with canti lever SI-DF20 (SII nanotechnology Co. Ltd., spring modulus: 15 N/m, radii of tip: 10 nm, scanning area: 2 μm × 2 μm).

X-ray diffraction measurements were carried out with RINT2000 (Rigaku Co. Ltd., 40 kV, 20 mA, X-ray source: CuKα ($\lambda = 1.5418$ Å) scanning rate: 1/min, sampling steps: 0.02°, scanning region: $2\theta = 5°-55°$) . The crystallite sizes were estimated from Scherrer's equation (1)

$$D = \frac{\lambda}{\beta \cos\theta} \qquad (1)$$

$$\beta^2 = B^2 - b^2 \qquad (2)$$

where D is the crystallite size, λ is the wavelength of X-ray beam, θ is the Bragg angle, B is the integral width of samples and b is that of silicon. In addition, the crystallinity of cellulose was calculated through the equation (3)
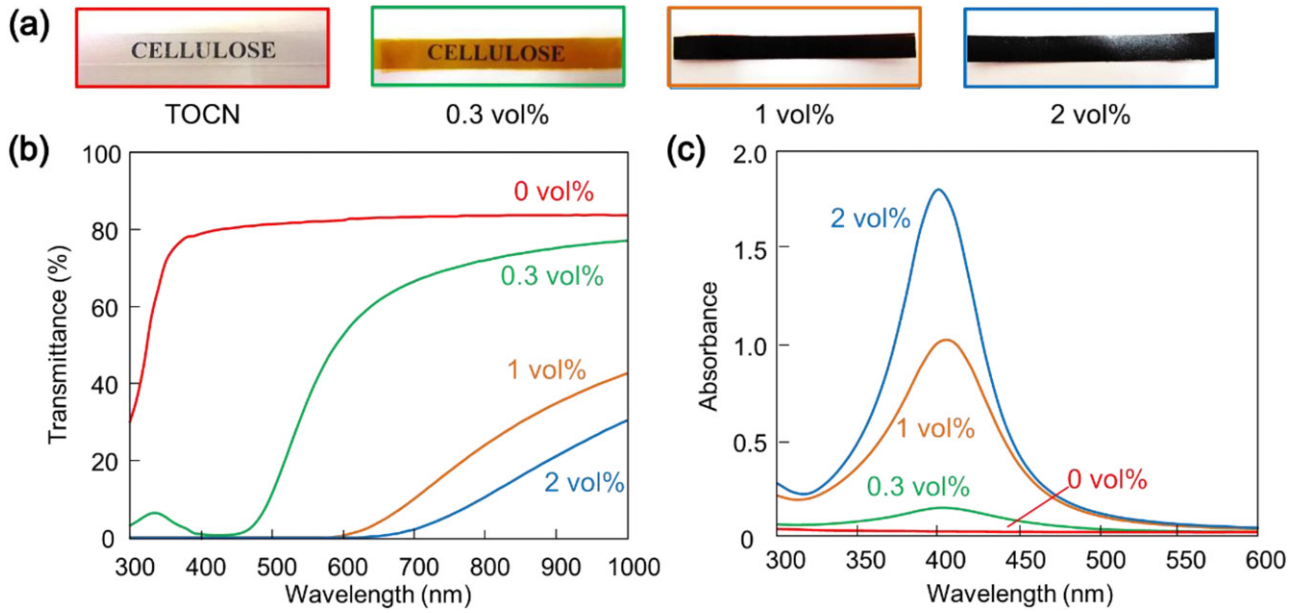
Figure 2. (a) Photographs and (b) UV-vis transmittance of TOCN and TOCN/AgNP nanocomposites with different silver contents (Thickness; 50 μm) and (c) absorbance spectra of TOCN/AgNP aqueous dispersion with different silver contents.

$$X_c = \frac{A_c}{A_c + A_a} \times 100 \qquad (3)$$

where X_c is the crystallinity, A_c is the area of the peaks originated from crystalline, and A_a is that of amorphous. For the measurements of the transmittance of the cellulose nanocomposite sheets (thickness: 50 μm), we measured the transmit spectra from 200 to 1000 nm with HITACHI U-2000. In UV–vis absorption measurement, we measured the aqueous dispersion including 0.25 wt% TOCN and AgNP.

For the investigation of thermal properties of TOCN/AgNP nanocomposites, we measured melting points of AgNP in nanocomposites under nitrogen with RIGAKU DSC8230. The scan rate was 5 °C/min. From the Gibbs–Thomson equation (4), the size of AgNP were estimated.

$$T = T_{\text{bulk}} - \frac{4\sigma M T_{\text{bulk}}}{\Delta H_m r \rho} \qquad (4)$$

where T and T_{bulk} (1223 K) are melting points of silver nanoparticles in nanocomposites and bulk silver, σ (1.02 J/m^2) is the solid-liquid interface energy, M (107.9 g/mol) is molecular weight, ΔH_m (11.3 kJ/mol) is the latent heat of fusion, r is the radii of silver nanoparticles and ρ (10.5 g/cm^3) is the density.

For thermogravimetric analysis of TOCN and TOCN/AgNP nanocomposites, we carried with RIGAKU Thermo plus EVO II TG8121 under nitrogen. The heating rate was 10 °C/min. The starting temperature was 150 °C for exclusion of effects of water.

The length and width of the trimmed samples for tensile tests were 40 and 5 mm, and they were dried at 40 °C for 24 h before tensile tests. We carried out with Autograph AGS-1kND (SHIMAZU Co. Ltd.). The strain-stress curves were obtained with 20 mm as initial lengths and 1 mm/min of the tensile speed. The density of TOCN was calculated by the floatation method. The initial inclination of the curves was regarded as Young's modulus.

For the measurement of the volume electric resistance of TOCN sheets and TOCN/AgNP nanocomposites, we measured with Electrometer/High Resistance Meter B2980A and Resistivity Cell 16008B (Keysight technologies Co. Ltd.) in the two ring electrode method. The diameter of the electrode was 26 mm and the applied voltage was 10 V.

For the evaluation of specific heat capacities of TOCN sheets and TOCN/AgNP nanocomposites, we performed with RIGAKU DSC8230. 10 mg Al$_2$O$_3$ was used as a standard sample. From the following equation (5), the specific heat capacity was calculated.

$$C_{\text{ps}} = \frac{C_{\text{pr}} \times m_r}{Y_r} \times \frac{Y_s}{m_s} \qquad (5)$$

where C_{ps}, C_{pr} are the specific heat capacities of TOCN/AgNP samples and Al$_2$O$_3$ standard, and m_s m_r are their weights. Y_s means the difference between the DSC curves of samples and empty Al pan, and Y_r is that between Al$_2$O$_3$ standard and empty Al pan.

For the measurement of the thermal diffusivity by the periodic heating and infrared radiation thermometer method, we carried with Thermowave Analyzer TA3 (Bethel Co. Ltd.). The thermal diffusivity for the in-plane and thickness directions was measured; in-plane means the parallel direction to the sheet surface and thickness means perpendicular one.
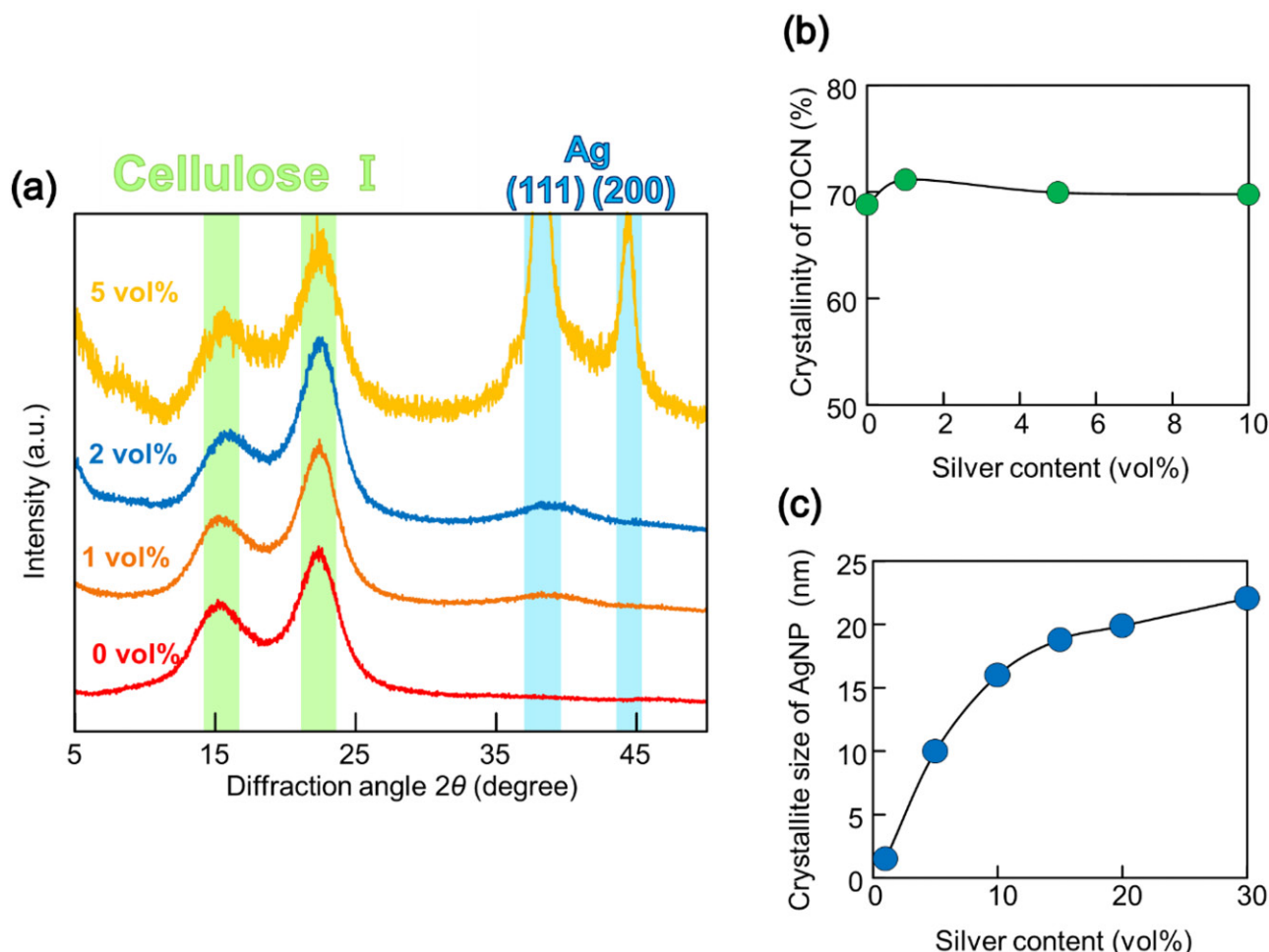
Figure 3. (a) X-ray diffraction pattern of TOCN and TOCN/AgNP nanocomposites. (b) Crystallinity of cellulose and (c) silver nanoparticle size in TOCN and TOCN/AgNP nanocomposites with different silver contents.

Results and discussion

We prepared a refined pulp from Kenaf bast fiber through degreasing, Wise treatment and alkaline treatment for removing grease, lignin and hemicellulose, respectively. The refined pulps were fibrillated to nanofibers by TEMPO-catalyst oxidation and fibrillation with Blender. The radii of TOCN were less than 5 nm from the AFM topological images in Figure 1. The amount of the carboxyl group of TOCN were 1.28 mmol/g from the measurements of conductometric titration and the degree of oxidation per anhydroglucose unit of cellulose (DO) was 0.21 [25, 26, 56, 57]. (Supplementary Figure S2) The silver nitrate aqueous solution was added into the obtained 0.25 wt% TOCN dispersion and stirred until ion exchange from sodium ions to silver ions. Following that, the equal amounts of sodium borohydride solution was added and silver ions were reduced to AgNPs. The reduced AgNPs possessed radii less than 5 nm and were aligned along the TOCN as shown in Figure 1. These alignments suggested that Ag ions would be chelated to the carboxyl groups of TOCN and reduced on the TOCN selectively rather than randomly [58]. In the

case of the TOCN/20 vol%AgNP composites, the free AgNPs were observed as shown in Supplementary Figure S3. This means that there were too much non-chelated silver ions to form the nuclei of nanoparticle along only the TOCN. In the FT-IR spectra, all the TOCN and TOCN/AgNP nanocomposites showed larger carbonyl stretching bands at around 1600 cm^{-1} than Kenaf microfibers, while there was no changed in the vibration bands of glucopyranose rings (1060 cm^{-1}). The latter indicated that polysaccharide structures of cellulose were sustained even after the TEMPO-oxidation and the reduction of Ag ions, as shown in Supplementary Figure S4.

The TOCN/AgNP nanocomposite sheets were prepared by filtration and dried over at 40 °C for 12 h under vacuum. Optical photographs and transmittance spectra of TOCN/AgNP composites and absorption spectra of the TOCN/AgNP aqueous dispersion were shown in Figure 2. TOCN sheets without AgNPs showed high transparency. With the increase of AgNP loading, the sheets turned brownish because of the surface plasmon resonance (SPR) of AgNPs [59]. In the absorption spectra of the
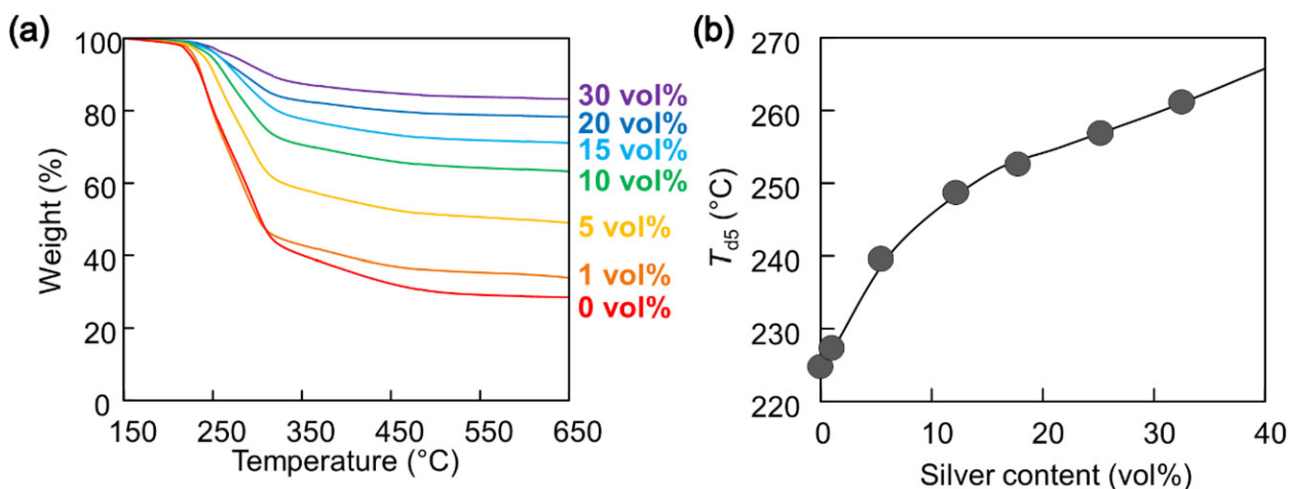
Figure 4. (a) Thermo-gravimetric traces and (b) thermal decomposition temperature with 5%wt loss of TOCN and TOCN/AgNP nanocomposites with different silver contents.

TOCN/AgNP suspensions, the absorption bands originated from SPR of AgNPs were observed at around 400 nm. These absorption bands were attributed to the AgNPs with less radii than 10 nm. This result corresponded to the size of AgNPs in the AFM images. In addition, this means that the AgNPs were highly dispersed in the TOCN aqueous dispersion without agglomeration [55, 60–62].

The X-ray diffraction measurements were performed for the TOCN and TOCN/AgNP nanocomposites. In their X-ray diffraction profiles in Figure 3a, all the samples showed the peaks originated from $1\bar{1}0$, 110, and 200 reflections of the cellulose I_β crystallites. The crystallinity of TOCN in composites was calculated in the area method, as shown in Figure 3b. The effects of the reductive reaction for the preparation of AgNPs were observed and their structure of cellulose I_β were maintained. The 111 and 200 reflections of AgNPs were appeared at $2\theta = 38°$ and $45°$ respectively with the loading of AgNPs in TOCN/AgNP nanocomposites. There is no diffraction peak assigned as silver oxide, such as (111) plane ($2\theta = 33°$) [63]. In addition, the crystallite sizes of AgNPs in TOCN/AgNP nanocomposites were estimated from the integral width and the Bragg angle using Scherrer's equation. As shown in Figure 3c, with the increase of loading amounts of AgNPs, the crystallite size of AgNPs was increased. In particular, AgNPs size in less than 5 vol% AgNPs composites were below 10 nm. These results also supported the nanosized silver particles in the composites.

The thermogravimetric curves of TOCN and TOCN/AgNPs nanocomposites were shown in Figure 4a. Above around 220 °C, the thermal weight loss drastically increased in all the samples. These thermal decomposition were attributed to the decomposition of TOCN. In this study, temperature at 5 wt% loss of TOCN/AgNP nanocomposites was defined as a decomposition temperature T_{d5}. T_{d5} were increased with the amounts of AgNP in the composites, as shown in Figure 4b. The loading of AgNP led to the higher thermal stability of TOCN matrix in their nanocomposites. The amounts of residues after thermal decomposition were increased as the loading of AgNPs increased. We calculated the amounts of AgNPs from the residues as shown in Supplementary Table S2.

For investigation of thermal behavior of AgNPs in nanocomposites, we measured their differential scanning calorimetry (DSC). It is known that the metallic nanoparticles possess lower melting points than bulk metals due to their higher specific surface areas [64]. In our nanocomposites, the melting point of only the 2 vol% AgNP nanocomposite was observed at 168 °C, which were lower than that (962 °C) of bulk silver. The radius of AgNP, which was estimated from the Gibbs-Thomson equation [65,66], was 5.8 nm. From all the various measurements such as AFM images, UV–vis absorption spectra, X-ray diffraction profiles and DCS thermograms, the AgNPs in the TOCN/AgNP nanocomposites were sustained as nanoparticles even through reduction reaction.

Figure 5a shows the results of tensile tests of Kenaf microfiber, TOCN sheets and TOCN/AgNP nanocomposites. Compared with the Kenaf microfiber sheet, downsizing of fiber diameter of TOCN led to the increase of the Young's modulus. The reason was that the mechanical defects of the nanofibers were decreased relative to microfibers. For the TOCN/AgNP composites, the low content ratios of the AgNPs provided the effective increase of mechanical modulus, whereas the modulus of the composites with larger content of AgNPs were decreased due to the agglomeration of AgNPs. In Figure 5b, the relationship between the AgNP loading and Young's modulus was represented as a solid line
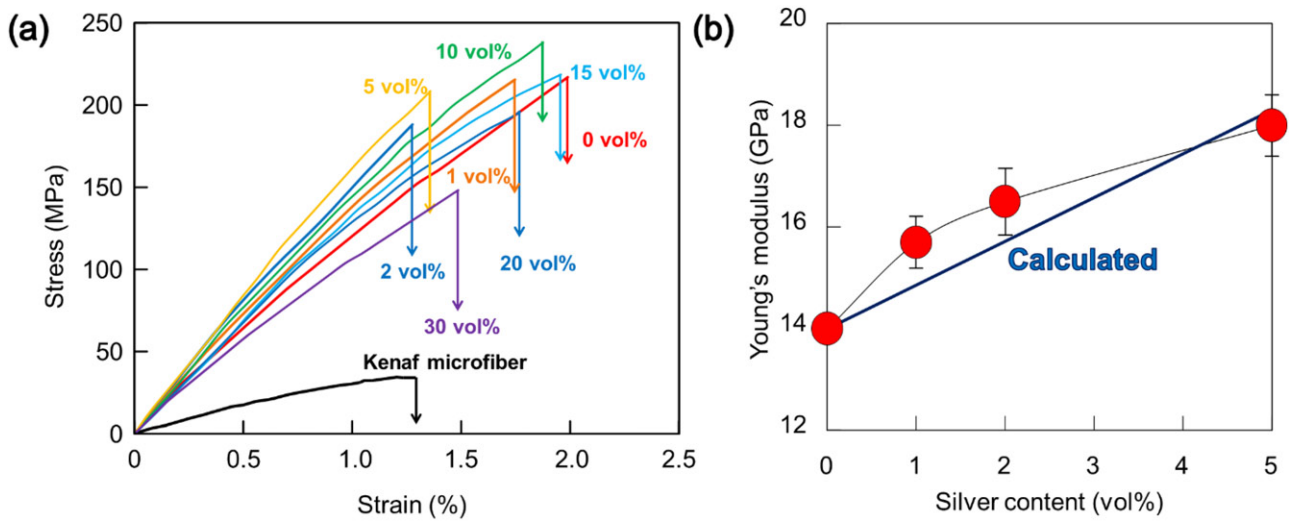
Figure 5. (a) Stress-strain curves of kenaf microfiber, TOCN and TOCN/AgNP nanocomposites with different silver contents. (b) Relationship between observed Young's modulus and silver content of TOCN/AgNP nanocomposites.
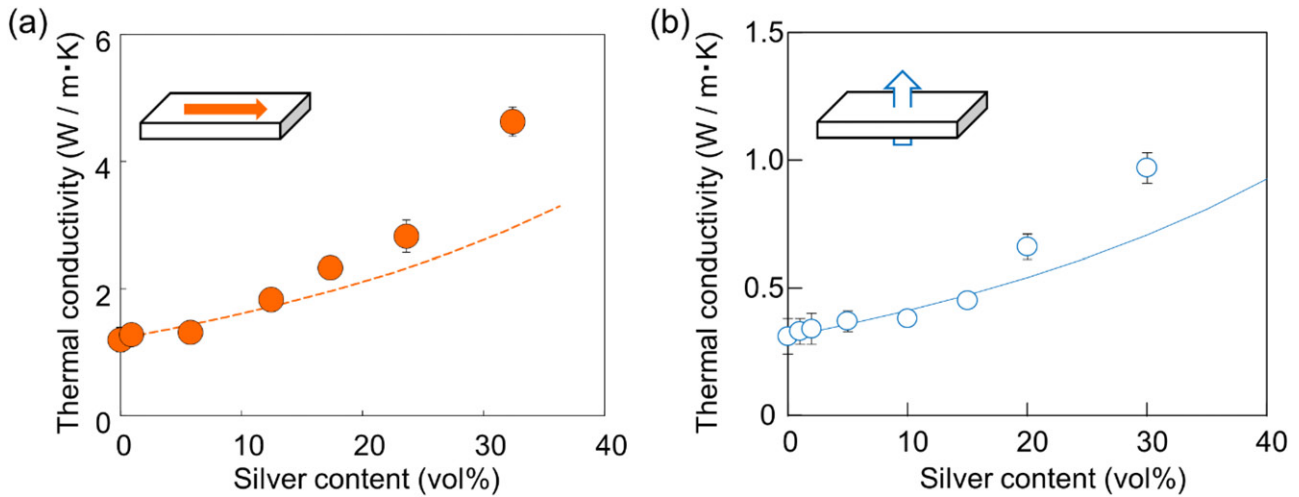

Figure 6. Thermal conductivity (circles: observed, lines: calculated) of TOCN/AgNP nanocomposites with different silver contents in (a) in-plane and (b) thickness direction.

and Young's modulus predicted by parallel model equation (6) as an upper bound was shown as a dashed line.

$$E_c = E_f V_f + E_m (1 - V_f) \qquad (6)$$

where E_c, E_f, and E_m are the modulus of the composites, fillers and matrix, respectively, and V_f is the volume fraction of fillers. The modulus of bulk silver (83 GPa) [67] and TOCN were applied as their modulus E_f and E_m, respectively. At the lower loading of AgNPs, the larger Young's modulus was exhibited than the estimated value. Moreover, the increase of amount of AgNPs led to higher densities of the composites, which suggested that the void would not emerge. These larger Young's modulus would be induced by the effect that the nano-sized AgNP possessed the higher modulus than the bulk silver [68, 69]. In contrast, the relation between the tensile strength or elongation at break of those composites and the AgNP fraction was not observed

clearly. The reason is that their mechanical parameters received large effects of the reinforcement as well as mechanical defects in the composites. In only the case of the composites with 30 vol% AgNP, it is obviously revealed that the excess AgNP additive led to the decrease of tensile strength or elongation at break.

It is well-known that silver possesses the highest thermal conductivity in single metals [67]. Therefore, we investigated the thermal conductivities of TOCN/AgNP nanocomposites and declared the loading effects of AgNPs. From the DSC measurements and thermal diffusion measurements, their specific heat (C_p) and the thermal diffusivities to the in-plane ($\alpha_{in\text{-}plane}$) and thickness (α_{thick}) direction were evaluated. The thermal conductivities ($\lambda_{in\text{-}plane}$ and λ_{thick}) were calculated from their parameters, as shown in Figure 6. In the TOCN sheets without AgNPs, the anisotropic thermal conductivity in the in-plane and thickness directions were emerged. In
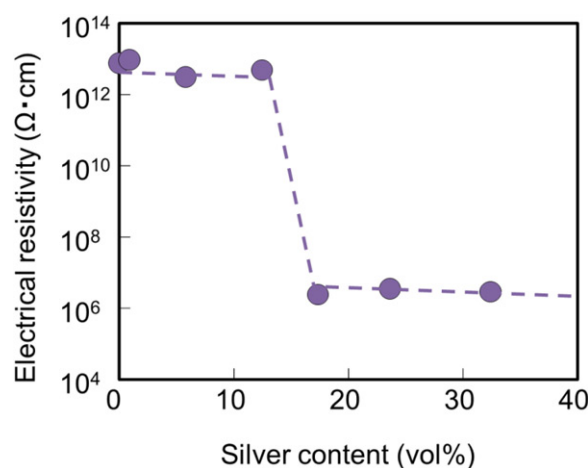
Figure 7. Electrical resistivity of TOCN and TOCN/AgNP nanocomposites.

the TOCN sheets, the TOCNs were oriented in the direction parallel to the sheet plane because of the vacuum filtration of TOCN aqueous dispersion. The AgNP loading increased the thermal conductivities to the in-plane direction ($\lambda_{\text{in-plane}}$). From the theory on the thermal conductivities of composite materials, namely the Maxwell equation (7), we calculated the theoretical thermal conductivities of the TOCN/AgNP nanocomposites.

$$\lambda_c = \lambda_m \frac{2\lambda_m + \lambda_f + 2V_f(\lambda_f + \lambda_m)}{2\lambda_m + \lambda_f - V_f(\lambda_f + \lambda_m)} \qquad (7)$$

where λ_c, λ_f, and λ_m are the thermal conductivities of the composite, filler and matrix, respectively, and V_f is the volume fraction of filler. The reported value of the thermal conductivity of AgNP filler (λ_f) is 430 W/m·K [70] and the experimental value of TOCN sheet is employed as the thermal conductivity of the matrix. In the Maxwell theory, it is assumed that the fillers were well-dispersed in the matrix and there was no interaction between the fillers [71]. In Figure 6, the theoretical and experimental thermal conductivities of the TOCN/AgNP nanocomposites were represented. At the low content ratios of the AgNPs, their thermal conductivities were increased in agreement with the Maxwell theory. These results indicated that the AgNPs were distributed homogeneously in the composites without any mutual interaction. In contrast, the nanocomposites with high content ratios of the AgNPs provided the higher thermal conductivities than the calculated values. This suggests that larger amounts of the AgNPs caused the contact of each other in the TOCN matrix and the formation of the thermal conductive paths. In the case of the thermal conductivities in the thickness direction, the nanocomposites including the high amounts of the AgNPs also demonstrated the higher thermal conductivities, whereas the values were much lower than those in the in-plane direction. The difference between the conductivities in the thickness and in-plane directions were attributed to the in-plane alignment of the TOCN and the AgNP in the nanocomposites.

The electrical resistance of the TOCN/AgNP nanocomposites was shown in Figure 7. In the region of the lower content ratios of the AgNP than 15 vol%, the high resistance of the nanocomposites kept constants regardless of the amount of the AgNP fillers. These high resistances were originated from electric insulation of the TOCN matrix. On the other hand, the drastically lower resistances were achieved in the nanocomposites with higher content ratios of the AgNP than 15 vol%. It is suspected that the AgNP fillers were contacted with one another and the conductive paths were formed by the percolation. The volume of the AgNP where the percolation in electrical resistance corresponded to those of thermal conductive percolation. Even in the larger amounts of AgNPs, the decrease of the electrical resistivity were incredibly slight. The reason was that the conductive paths have been formed and the additional AgNP fillers had no large effect on their electrical resistance. The gained electrical resistance of the TOCN/AgNP nanocomposites were compared with those of general semiconductors [72–74].

Conclusions

We demonstrated the preparation of the TOCN/AgNP nanocomposites and achieved the functionalization of TOCN nanopapers. The AgNPs were formed through the chelation of Ag ions to carbonyl groups of TOCN, then reduction in aqueous dispersion. The sizes of the AgNPs were less than 10 nm and the nanoparticles were well dispersed in nanocomposites. The AgNPs in the nanocomposites were aligned along the TOCN. The loading of AgNPs increased thermal stabilities of nanocomposites and their mechanical properties. In addition, their thermal conductivities emerged anisotropy between in-plane and thickness direction. With high loading of AgNPs, the higher thermal and electrical conductivities were accessed by their percolation.

Disclosure statement

The authors declare no competing financial interest.

Notes on contributors

Hiroaki Ito is a graduated student in the departments of chemical science and engineering at Kobe University. He has worked on thermal and electrical conductivities of cellulose nanofiber composites with silver nanomaterials.

Mibuki Sakata is a graduated student in the departments of chemical science and engineering at Kobe University. She has worked on poly methyl methacrylate / cellulose nanofiber composites and effect of their interaction on mechanical and thermal properties.

Chizuru Hongo is an assistant professor in the departments of chemical science and engineering at Kobe University. She has published on the properties and structure of collagen.

Takuya Matsumoto is an assistant professor in the departments of chemical science and engineering at Kobe University. He has published on the synthesis of polymers and properties of polymer surface and interface.

Takashi Nishino is a professor in the departments of chemical science and engineering at Kobe University. He has published on the structure and mechanical properties of polymers and nanocomposites, interface interaction between matrix and filler, and adhesion of polymers.

References

1. Nishino T, Peijs T. All-cellulose composites. Vol. 5, Handbook of green materials. World Scientific; 2013. p. 201–216.
2. Nishino T, Takano K, Nakamae K. Elastic modulus of the crystalline regions of cellulose polymorphs. J Polym Sci B Polym Phys. 1995;33:1647–1651.
3. Fukuzumi H, Saito T, Iwata T, et al. Transparent and high gas barrier films of cellulose nanofibers prepared by TEMPO-mediated oxidation. Biomacromolecules. 2009;10:162–165.
4. Wu C-N, Saito T, Fujisawa S, et al. Ultrastrong and high gas-barrier nanocellulose/clay-layered composites. Biomacromolecules. 2012;13:1927–1932.
5. Isogai A, Hänninen T, Fujisawa S, et al. Review: Catalytic oxidation of cellulose with nitroxyl radicals under aqueous conditions. Prog Polym Sci. 2018;86:122–148.
6. Bhatnagar A, Sain M. Processing of cellulose nanofiber-reinforced composites. J Reinf Plast Compos. 2005;24:1259–1268.
7. Iwatake A, Nogi M, Yano H. Cellulose nanofiber-reinforced polylactic acid. Compos Sci Technol. 2008;68:2103–2106.
8. Jonoobi M, Harun J, Mathew AP, et al. Mechanical properties of cellulose nanofiber (CNF) reinforced polylactic acid (PLA) prepared by twin screw extrusion. Compos Sci Technol. 2010;70:1742–1747.
9. Sehaqui H, Zhou Q, Ikkala O, et al. Strong and tough cellulose nanopaper with high specific surface area and porosity. Biomacromolecules. 2011;12:3638–3644.
10. Nogi M, Iwamoto S, Nakagaito AN, et al. Optically transparent nanofiber paper. Adv Mater. 2009;21:1595–1598.
11. Peresin MS, Habibi Y, Zoppe JO, et al. Nanofiber composites of polyvinyl alcohol and cellulose nanocrystals: manufacture and characterization. Biomacromolecules. 2010;11:674–681.
12. Zhu H, Li Y, Fang Z, et al. Highly thermally conductive papers with percolative layered boron nitride nanosheets. ACS Nano. 2014;8:3606–3613.
13. Ho TTT, Zimmermann T, Ohr S, et al. Composites of cationic nanofibrillated cellulose and layered silicates: water vapor barrier and mechanical properties. ACS Appl Mater Interfaces. 2012;4:4832–4840.
14. Gao K, Shao Z, Wu X, et al. Cellulose nanofibers/reduced graphene oxide flexible transparent conductive paper. Carbohydr Polym. 2013;97:243–251.
15. Ji S, Jang J, Cho E, et al. High dielectric performances of flexible and transparent cellulose hybrid films controlled by multidimensional metal nanostructures. Adv Mater. 2017;29:1700538.
16. Nogi M, Karakawa M, Komoda N, et al. Transparent conductive nanofiber paper for foldable solar cells. Sci Rep. 2015;5:17254.
17. Fujisaki Y, Koga H, Nakajima Y, et al. Transparent nanopaper-based flexible organic thin-film transistor array. Adv Funct Mater. 2014;24:1657–1663.
18. Nogi M, Kim C, Sugahara T, et al. High thermal stability of optical transparency in cellulose nanofiber paper. Appl Phys Lett. 2013;102:181911.
19. Ghaderi M, Mousavi M, Yousefi H, et al. All-cellulose nanocomposite film made from bagasse cellulose nanofibers for food packaging application. Carbohydr Polym. 2014;104:59–65.
20. Amini E, Azadfallah M, Layeghi M, et al. Silver-nanoparticle-impregnated cellulose nanofiber coating for packaging paper. Cellulose. 2016;23:557–570.
21. Klemm D, Schumann D, Kramer F, et al. Nanocelluloses as innovative polymers in research and application BT – polysaccharides II. D. Klemm, editor. Springer Berlin Heidelberg; 2006. p. 49–96.
22. Bhattacharya M, Malinen MM, Lauren P, et al. Nanofibrillar cellulose hydrogel promotes three-dimensional liver cell culture. J Control Release. 2012;164:291–298.
23. Taniguchi T, Okamura K. New films produced from microfibrillated natural fibres. Polym Int. 1998;47:291–294.
24. Nakagaito AN, Yano H. Cellulose-nanofiber-based materials. In: J. P. Hinestroza, A. N. Netravali, editors. Chapter 1, Cellulose based composites: new green nanomaterials. Wiley; 2014.
25. Okita Y, Saito T, Isogai A. Entire surface oxidation of various cellulose microfibrils by TEMPO-mediated oxidation. Biomacromolecules. 2010;11:1696–1700.
26. Saito T, Kimura S, Nishiyama Y, et al. Cellulose nanofibers prepared by TEMPO-mediated oxidation of native cellulose. Biomacromolecules. 2007;8:2485–2491.
27. Saito T, Nishiyama Y, Putaux J-L, et al. Homogeneous suspensions of individualized microfibrils from TEMPO-catalyzed oxidation of native cellulose. Biomacromolecules. 2006;7:1687–1691.
28. Hussain F, Hojjati M, Okamoto M, et al. Review article: polymer-matrix nanocomposites, processing, manufacturing, and application: an overview. J Compos Mater. 2006;40:1511–1575.
29. Manias E, Touny A, Wu L, et al. Polypropylene/montmorillonite nanocomposites. Review of the synthetic routes and materials properties. Chem Mater. 2001;13:3516–3523.
30. Eichhorn SJ, Baillie CA, Zafeiropoulos N, et al. Review: current international research into cellulosic fibres and composites. J Mater Sci. 2001;36:2107–2131.

31. Merkel TC, Freeman BD, Spontak RJ, et al. Ultrapermeable, reverse-selective nanocomposite membranes. Science. 2002;296:519–522.

32. Yampolskii Y. Polymeric gas separation membranes. Macromolecules. 2012;45:3298–3311.

33. Huang X, Zhi C, Jiang P, et al. Polyhedral oligosilsesquioxane-modified boron nitride nanotube based epoxy nanocomposites: an ideal dielectric material with high thermal conductivity. Adv Funct Mater. 2013;23:1824–1831.

34. Szabó T, Szeri A, Dékány I. Composite graphitic nanolayers prepared by self-assembly between finely dispersed graphite oxide and a cationic polymer. Carbon. 2005;43:87–94.

35. Hu G, Zhao C, Zhang S, et al. Low percolation thresholds of electrical conductivity and rheology in poly(ethylene terephthalate) through the networks of multi-walled carbon nanotubes. Polymer. 2006;47:480–488.

36. Gojny FH, Wichmann MHG, Fiedler B, et al. Evaluation and identification of electrical and thermal conduction mechanisms in carbon nanotube/epoxy composites. Polymer. 2006;47:2036–2045.

37. Bockstaller MR, Mickiewicz RA, Thomas EL. Block copolymer nanocomposites: perspectives for tailored functional materials. Adv Mater. 2005;17:1331–1349.

38. Sanchez C, Lebeau B, Chaput F, et al. Optical properties of functional hybrid organic–inorganic nanocomposites. Adv Mater. 2003;15:1969–1994.

39. Liu J, Ueda M. High refractive index polymers: fundamental research and practical applications. J Mater Chem. 2009;19:8907–8919.

40. Chang C-C, Chen W-C. Synthesis and optical properties of polyimide-silica hybrid thin films. Chem Mater. 2002;14:4242–4248.

41. Pradhan N, Pal A, Pal T. Silver nanoparticle catalyzed reduction of aromatic nitro compounds. Colloids Surf A Physicochem Eng Asp. 2002;196:247–257.

42. Mitsudome T, Mikami Y, Funai H, et al. Oxidant-free alcohol dehydrogenation using a reusable hydrotalcite-supported silver nanoparticle catalyst. Angew Chem Int Ed. 2008;47:138–141.

43. Sarina S, Waclawik ER, Zhu H. Photocatalysis on supported gold and silver nanoparticles under ultraviolet and visible light irradiation. Green Chem. 2013;15:1814–1833.

44. Pourreza N, Golmohammadi H, Naghdi T, et al. Green in-situ synthesized silver nanoparticles embedded in bacterial cellulose nanopaper as a bionanocomposite plasmonic sensor. Biosens Bioelectron. 2015;74:353–359.

45. Lombardi JR, Birke RL. A unified view of surface-enhanced raman scattering. Acc Chem Res. 2009;42:734–742.

46. Schlücker S. Surface-enhanced Raman spectroscopy: concepts and chemical applications. Angew Chem Int Ed. 2014;53:4756–4795.

47. Moon K-S, Dong H, Maric R, et al. Thermal behavior of silver nanoparticles for low-temperature interconnect applications. J Electron Mater. 2005;34:168–175.

48. Park M, Im J, Shin M, et al. Highly stretchable electric circuits from a composite material of silver nanoparticles and elastomeric fibres. Nat Nanotech. 2012;7:803–809.

49. Hu R, Li G, Jiang Y, et al. Silver–Zwitterion organic–inorganic nanocomposite with antimicrobial and antiadhesive capabilities. Langmuir. 2013;29:3773–3779.

50. Cai S, Pourdeyhimi B, Loboa EG. High-throughput fabrication method for producing a silver-nanoparticles-doped nanoclay polymer composite with novel synergistic antibacterial effects at the material interface. ACS Appl Mater Interfaces. 2017;9:21105–21115.

51. Lokanathan AR, Uddin KMA, Rojas OJ, et al. Cellulose nanocrystal-mediated synthesis of silver nanoparticles: role of sulfate groups in nucleation phenomena. Biomacromolecules. 2014;15:373–379.

52. Wu M, Kuga S, Huang Y. Quasi-one-dimensional arrangement of silver nanoparticles templated by cellulose microfibrils. Langmuir. 2008;24:10494–10497.

53. Yu J, Liu RYF, Poon B, et al. Polymers with palladium nanoparticles as active membrane materials. J Appl Polym Sci. 2004;92:749–756.

54. Ifuku S, Tsuji M, Morimoto M, et al. Synthesis of silver nanoparticles templated by TEMPO-mediated oxidized bacterial cellulose nanofibers. Biomacromolecules. 2009;10:2714–2717.

55. Cai J, Kimura S, Wada M, et al. Nanoporous cellulose as metal nanoparticles support. Biomacromolecules. 2009;10:87–94.

56. Isogai A, Saito T, Fukuzumi H. TEMPO-oxidized cellulose nanofibers. Nanoscale. 2011;3:71–85.

57. Isogai T, Yanagisawa M, Isogai A. Degrees of polymerization (DP) and DP distribution of cellouronic acids prepared from alkali-treated celluloses and ball-milled native celluloses by TEMPO-mediated oxidation. Cellulose. 2009;16:117–127.

58. Zhang T, Wang W, Zhang D, et al. Biotemplated synthesis of gold nanoparticle–bacteria cellulose nanofiber nanocomposites and their application in biosensing. Adv Funct Mater. 2010;20:1152–1160.

59. Paramelle D, Sadovoy A, Gorelik S, et al. A rapid method to estimate the concentration of citrate capped silver nanoparticles from UV-visible light spectra. Analyst. 2014;139:4855–4861.

60. Kreibig U, Genzel L. Optical absorption of small metallic particles. Surf Sci. 1985;156:678–700.

61. Sone A, Saito T, Isogai A. Preparation of aqueous dispersions of TEMPO-oxidized cellulose nanofibrils with various metal counterions and their super deodorant performances. ACS Macro Lett. 2016;5:1402–1405.

62. Ferraria AM, Boufi S, Battaglini N, et al. Hybrid systems of silver nanoparticles generated on cellulose surfaces. Langmuir. 2010;26:1996–2001.

63. Dhoondia ZH, Chakraborty H. Lactobacillus mediated synthesis of silver oxide nanoparticles. Nanomater Nanotechnol. 2012;2:15.

64. Gladkich NT, Niedermayer R, Spiegel K. Nachweis großer Schmelzpunktserniedrigungen bei dünnen Metallschichten. Phys Stat Sol (b). 1966;15:181–192.

65. Johnson CA. Generalization of the Gibbs-Thomson equation. Surf. Sci. 1965;3:429–444.

66. MA, GB. McKenna Effects of confinement on material behaviour at the nanometre size scale. J Phys Condens Matter. 2005;17:R461.

67. Li X, Gao H, Murphy CJ, et al. Nanoindentation of silver nanowires. Nano Lett. 2003;3:1495–1498.

68. Gou J-G, Zhou L-J, Zhao Y-P. Size-dependent elastic modulus and fracture toughness of the nanofilm with surface effects. Surf Rev Lett. 2008; 15:599–603.

69. Liang LH, Li JC, Jiang Q. Size-dependent elastic modulus of Cu and Au thin films. Solid State Commun. 2002;121:453–455.

70. Bjorneklett A, Halbo L, Kristiansen H. Thermal conductivity of epoxy adhesives filled with silver particles. Int J Adhes. 1992;12:99–104.

71. Jiajun W, Xiao-Su Y. Effects of interfacial thermal barrier resistance and particle shape and size on the thermal conductivity of AlN/PI composites. Compos Sci Technol. 2004;64:1623–1628.

72. Kanatzidis MG, Bissessur R, DeGroot DC, et al. New intercalation compounds of conjugated polymers. Encapsulation of polyaniline in molybdenum disulfide. Chem Mater. 1993;5:595–596.

73. Chen SA, Ni JM. Structure/properties of conjugated conductive polymers. 1. Neutral poly(3-alkythiophene)s. Macromolecules. 1992;25:6081–6089.

74. Hsieh BR, Wei Y. Electroplastics for plastic electronics. Vol. 735, Semiconducting Polymers. American Chemical Society, 1999. p. 1.